Korean J. Chem. Eng., 32(6), 1046-1059 (2015)
DOI: 10.1007/s11814-014-0327-5

pISSN: 0256-1115
eISSN: 1975-7220

Chemical reaction effect on double diffusive convection in porous media with magnetic and variable gravity effects

Akil Jassim Harfash*,† and Ahmed Kadhim Alshara**

*Department of Mathematics, College of Sciences, University of Basrah, Basrah, Iraq
**Petroleum department, College of Engineering, University of Misan, Misan, Iraq
(*Received 10 September 2014 • accepted 4 November 2014*)

Abstract−We study the problem of double diffusive convective movement of a reacting solute in a viscous incompressible occupying a plane layer in a saturated porous medium and subjected to a vertical magnetic field. The thresholds for linear instability are found and compared to those derived by a global nonlinear energy stability analysis. Then, the accuracy of both the linear instability and global nonlinear energy stability thresholds are tested using a three dimensional simulation. The strong stabilizing effect of gravity field and magnetic field is shown. Moreover, the results support the assertion that the linear theory, in general, is accurate in predicting the onset of convective motion, and thus, regions of stability.

Keywords: Double-diffusive Convection, Chemical Reaction, Magnetic Field, Variable Gravity, Subcritical Instability, Finite Differences

INTRODUCTION

Penetrative convection refers to a convective motion, where part of the layer has a tendency to be unstable, which then induces instability in the rest of the layer (cf. Nield and Bejan [1]). One of the most widely employed mechanisms to describe penetrative convection is internal heating. An internal heat source (or sink) can give rise to a situation where one part of a layer is naturally convecting while the other remains stable, allowing penetrative convection to occur. Recently, mathematical models to describe penetrative convection have been developed and analyzed intensely by Ganesan and Suganthi [2], Hwang [3], Kim [4-6], Liu et al. [7], Lungu et al. [8], Nield and Kuznetsov [9-13], Sharma et al. [14] and Shojaeian and Shojaee [15].

Most available studies focus on the natural convection heat transfer through a porous medium saturated by an electrically nonconducting fluid, as in most practical situations. Recently, the equally important problem of hydromagnetic convective flow of a conducting fluid through a porous medium has been the center of much investigation. Subjected to a magnetic field, the motion of an electrically conducting fluid induces an electric current whose fluid velocity is reduced, in general, by interaction between the electric current and the motion. The natural convection of electrically conducting fluids in porous media where a magnetic field exists has not, however, been the subject of much research, although there are potential applications. An example is the study of the interaction of the geomagnetic field with the fluid in geothermal regions, where the Earth's crust functions as a porous medium is regarded by geophysicists as being of considerable importance. Also, with continuous casting, an example of metallurgical applications, electromagnetic stirring can improve the solidification structure to produce a fine-grained structure, with better final mechanical properties. Where dendritic solidification of alloys is concerned, dendrites in the mushy zone can be regarded as a porous medium. Some attention has been focussed on how a magnetic field affects the onset of instability in porous medium layers (cf. [16-20] and the references therein).

Double-diffusive flows in porous media are widely encountered both in nature and in technological processes [21]. Bioremediation, where micro-organisms are introduced to change the chemical composition of contaminants is a very topical area, cf. Chen et al. [22], Suchomel et al. [23]. Contaminant/pollution transport is yet another area of multi-component flow in porous media which is of much interest in environmental engineering, cf. Curran and Allen [24], Ewing and Weekes [25], Franchi and Straughan [26]. Other very important and topical areas of salt/heat transport in porous flows are in oil reservoir simulation, e.g. Ludvigsen et al. [27], and salinization in desert-like areas, Gilman and Bear [28].

In this study, we analyzed a model of double diffusive convection in a porous medium with chemical reaction, variable gravity field and magnetic field effects. Coupled heat and mass transfer problems in presence of chemical reaction are important in many processes and have, therefore, received considerable amount of attention. In drying, distribution of temperature and moisture over agricultural fields and groves of fruit trees, damage of crops due to freezing, evaporation at the surface of a water body, energy transfer in a wet cooling tower and flow in a desert cooler, heat and mass transfer occur simultaneously. Possible applications of this type of flow can be found in many industries. For instance, in the power industry, among the methods of generating electric power is one in which electrical energy is extracted directly from a moving conducting fluid. For more details on these application see [29], [30] and [31]

†To whom correspondence should be addressed.
E-mail: akilharfash@gmail.com

and references therein.

Modeling as realistically as possible these physical phenomena is the main impetus behind the extensive research into fluid mechanics. The mathematical idealisation of the stability of these real world problems is achieved through the use of partial differential equations to model the physical problem. The study of the stability of such systems of partial differential equations is a key aspect in their physical interpretation (see e.g. Nield and Bejan [1] and Straughan [32]), and continues to be one of the most pursued topics in fluid mechanics. To find regions of stability we must use linear instability and nonlinear stability theories. Between the stability and instability boundaries, neither the linear nor nonlinear methods provide information about the stability; instead the equations must be solved using a three-dimensional computation. In some instances, nonlinear stability bounds obtained are far below the linear instability bounds and the region of unknown stability is large.

However, when the difference between the linear (which predicts instability) and nonlinear (which predicts stability) thresholds is very large, the accuracy of the linear instability threshold to capture the onset of the instability is unclear. Thus, we select a regions which have large subcritical instabiltiies and then develop a three-dimensional simulation for the problem to test the accuracy of these thresholds. To achieve this we transform the problem into **u**–curl(**u**) formulation and utilize second-order finite difference schemes. Recently, in [33-41], the accuracy of both the linear instability and global nonlinear energy stability thresholds was tested using three-dimensional simulations. Our results show that the linear threshold accurately predicts on the onset of instability in the basic steady state. However, the required time to arrive at the steady state increases significantly as the Rayleigh number tends to the linear threshold.

In the next section, we present the governing equations of motion and derive the associated perturbation equations. In Section 3, we introduce the linear and nonlinear analysis of our system. In Section 4, the numerical results for the linear theory and a direct comparison with those of the global nonlinear theories are presented. In Section 5, we transform our system to **u**–curl(**u**) formulation and introduce the numerical solution of the problem in three dimensions. The results of our numerical investigation are then compiled and discussed in the final section of the paper.

MATHEMATICAL FORMULATION AND GOVERNING EQUATIONS

Consider a layer Ω of a water saturated porous medium bounded by two horizontal planes as shown in Fig. 1. Let d>0, $\Omega=R^2=(0, d)$ and Oxyz be a Cartesian frame of reference with unit vectors i, j, k. Denoting v, T and C to be the velocity, temperature and concentration of the dissolved species. The porous medium in the box with porosity ε. The fluid is subjected to the buoyancy forces resulting from temperature difference (T_L-T_U) and the diffusion of mass due to the concentration difference (C_L-C_U) between the upper and lower planes where $T_L>T_U$ and $C_L>C_U$, behind that the electromagnetic force resulting from convection of fluid in an uniform magnetic field. The diffusion in the box is unsteady and three-dimensional, subject to a uniform magnetic field B. We assume that the

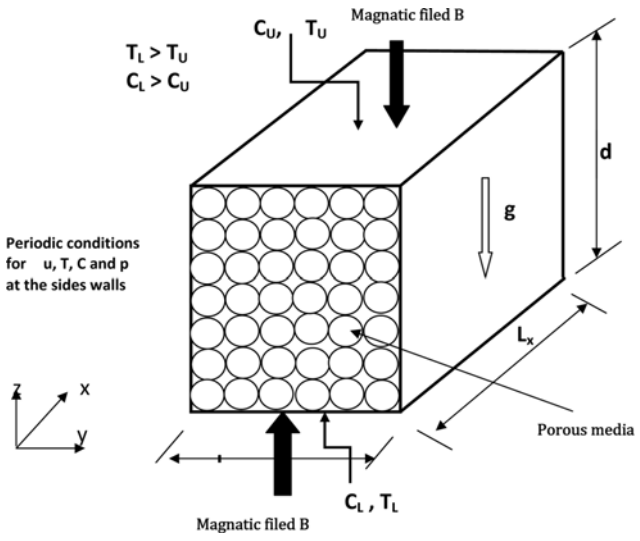

Fig. 1. A schematic of the physical domain.

variables (u, T, C and p) are periodic in the x and y directions with periodically cells. Also, assuming that the Oberbeck-Boussinesq approximation is valid (cf. [1] and [32] and references therein), the flow in the porous medium is governed by Darcy's law

$$\frac{\mu}{\kappa}v_i=-p_{,i}-k_i g(z)\rho(T, C)+\mathbf{j}\times\mathbf{B}, \tag{1}$$

$$v_{i,i}=0, \tag{2}$$

$$\frac{1}{M_1}T_{,t}+v_i T_{,i}=\kappa_t\nabla^2 T, \tag{3}$$

$$\varepsilon C_{,t}+v_i C_{,i}=\kappa_c\nabla^2 C-K_1(C-C_0), \tag{4}$$

where (2) is the incompressibility condition and (3) and (4) are the equations of energy and solute balance, respectively. The derivation of Eqs. (1)-(4) may be found in [1].

We have denoted p, μ, g, κ, C_0, K_1, **j** and κ_c to be the pressure, viscosity, gravitational acceleration, permeability of the porous medium, reference concentration, chemical reaction rate, current and salt diffusivity, respectively. The density ρ is of the form

$$\rho(T, C)=\rho_0(1-\alpha_t(T-T_0)+\alpha_c(C-C_0))$$

where ρ_0 and T_0 are a reference density and temperature, respectively, and α_t and α_c are the coefficients for thermal and solutal expansion, respectively.

The effective thermal conductivity of the saturated porous medium κ_t is defined by the ratio between the thermal diffusivity of the porous medium and the heat capacity per unit volume of the fluid:

$$\kappa_t=\frac{(1-\varepsilon)\kappa_s+\varepsilon\kappa_f}{(\rho_0 c_p)_f}$$

where κ_s and κ_f are the thermal diffusivities of the solid and fluid components of the porous medium, respectively and c_p is the specific heat of the fluid at constant pressure. The coefficient M_1 is the ratio of heat capacities defined by

$$M_1=\frac{(\rho_0 c_p)_f}{(\rho_0 c)_m}. \tag{5}$$

In (5) c is the specific heat of the solid, and

$$(\rho_0 c)_m=(1-\varepsilon)(\rho_0 c)_s+\varepsilon(\rho_0 c_p)_f,$$

denotes the overall heat capacity per unit volume of the porous medium. The subscripts f, s and m referring to the fluid, solid and porous components of the medium, respectively.

Convectional hydrodynamic stability theory is mainly concerned with the determination of critical values of Rayleigh number, demarcating a region of stability from that of instability. To make the convective overturning instability problem tractable we employ the quasi-static MHD approximation of Galdi and Straughan [42]. This assumes that the electric field, **E**, may be derived from a potential $E=-\nabla\chi$. The magnetic field **H** and the electric field satisfy Maxwell's equations, cf. Roberts [43], Fabrizio and Morro [44], so that

$$curl\mathbf{H}=\mathbf{j},\ \ curl\mathbf{E}=-\frac{\partial\mathbf{B}}{\partial t}.$$

Here $\mathbf{B}=\mu\mathbf{H}$ and then Galdi and Straughan [42] show that if the vertical component in the perturbed motion is zero in the limit the magnetic Prandtl number $P_m=\nu/\eta\to 0$, where η is the resistivity, then $\mathbf{j}\times\mathbf{B}$ in Eq. (1) may be replaced by

$$\mathbf{j}\times\mathbf{B}=\sigma_1(\mathbf{v}\times\mathbf{B}_0)\times\mathbf{B}_0, \tag{6}$$

where σ_1 is the electrical conductivity and $\mathbf{B}_0=(0, 0, B_0)$ is a magnetic field with only the vertical component. We now employ (6) in (1). The steady state, for which there is no fluid flow, is given by

$$\overline{v}_i\equiv 0,$$

$$\frac{d\overline{C}}{dz}=-\frac{\Delta C}{d}f\left(\frac{z}{d};\xi,\eta\right),$$

$$\overline{T}=-\beta z+T_L,$$

$$\frac{d\overline{p}}{dz}=-g(z)\rho(\overline{T},\overline{C}),$$

where

$$f\left(\frac{z}{d};\xi,\eta\right)=\frac{\xi}{\sinh(\xi)}\{1-\eta(1-\cosh(\xi))\}\cosh\left(\xi\frac{z}{d}\right)-\xi\eta\sinh\left(\xi\frac{z}{d}\right),$$

$$\xi=A_1 d,\ A_1^2=\frac{K_1}{\kappa_c},\ \Delta C=|C_L-C_U|,\ \Delta T=|T_L-T_U|,\ \eta=\frac{C_L}{\Delta C},\ \beta=\frac{\Delta T}{d}.$$

To investigate the stability of these solutions, we introduce perturbations (u_i, p, θ, ϕ) by

$$v_i=u_i+\overline{v}_i,\ p=P+\overline{p},\ T=\theta+\overline{T},\ C=\phi+\overline{C}.$$

The perturbation equations are nondimensionalized according to the scales (stars denote dimensionless quantities)

$$x=x^* d,\ t=t^*\frac{\rho_0\kappa}{\mu},\ u=Uu^*,\ \theta=T^{\#}\theta^*,\ \phi=C^{\#}\phi^*,\ P=PP^*,$$

$$C^{\#}=U\sqrt{\frac{\mu d\Delta C}{\rho_0\kappa_c\alpha_c\kappa}},\ R_c=\sqrt{\frac{\kappa\rho_0\alpha_c d\Delta C}{\mu\kappa_c}},\ T^{\#}=U\sqrt{\frac{d^2\mu\beta}{\kappa\rho_0\kappa_t\alpha_t}},$$

$$R_t=\sqrt{\frac{d^2\kappa\rho_0\beta\alpha}{\mu\kappa_t}},\ \hat{\varepsilon}=\frac{1}{\varepsilon},\ U=\frac{d\mu}{\kappa\rho_0},\ P=\frac{d\mu}{\kappa}U,$$

$$M=B_0\sqrt{\frac{\sigma_1\kappa}{\mu}},\ p_r=\frac{d^2\mu}{M_1\kappa\rho_0\kappa_t},\ p_s=\frac{\varepsilon d^2\mu}{\kappa\rho_0\kappa_c}.$$

where p_t and p_s are the thermal and solute Prandtl numbers and R_t^2 and R_c^2 are the thermal and solute Rayleigh numbers, respectively. The dimensionless perturbation equations are (after omitting all stars)

$$u_i=-p_{,i}+R_t k g(z)\theta-R_c k g(z)\phi+M^2[(u\times k)\times k]_i, \tag{7}$$

$$u_{i,i}=0, \tag{8}$$

$$p_r(q_{,t}+M_1 u_i q_{,i})=R_t w+\nabla^2\theta, \tag{9}$$

$$p_s(\phi_{,t}+\hat{\varepsilon}u_i\phi_{,i})=R_c f(z)w+\nabla^2\phi-\xi^2\phi, \tag{10}$$

with $w=u_3$ and

$$f(z)=\frac{\xi}{\sinh(\xi)}\{1+\eta(1-\cosh(\xi))\}\cosh(\xi z)+\xi\eta\sinh(\xi z).$$

These equations hold in the region $\{z\in(0, 1)\}\times\{(x, y)\in R^2\}$ and the boundary conditions to be satisfied are:

$$\mathbf{u}=0,\ \theta=0,\ \phi=0,\ \text{at } z=0, 1, \tag{11}$$

where u_i, p, θ and ϕ are assumed periodic in the x and y directions.

Remark 2.1 *We observe that as g(z)=1, M=0 and $x\to 0$, $f\to 1$, the chemical reaction term disappears and we recover the standard double diffusive convection problem. However, the presence of the f(z) term considerably complicates the linear instability/nonlinear stability analysis.*

LINEAR AND NONLINEAR ENERGY STABILITY THEORIES

To obtain the threshold for linear instability where we know convection occurs, we neglect the nonlinear terms in Eqs. (7)-(10). Then, due to linearity we may seek solutions like $u_i(\mathbf{x}, t)=u_i(\mathbf{x})e^{\sigma t}$, $\theta(\mathbf{x}, t)=\theta(\mathbf{x})e^{\sigma t}$, $\phi(\mathbf{x}, t)=\phi(\mathbf{x})e^{\sigma t}$ and $P(\mathbf{x}, t)=P(\mathbf{x})e^{\sigma t}$, where σ is a complex constant. This leads to the system

$$u_i=-\pi_{,i}+R_t g(z)\theta k_i-R_c g(z)\phi k_i+M^2[(\mathbf{u}\times\mathbf{k})\times\mathbf{k}]_i, \tag{12}$$

$$p_r\sigma\theta=\Delta\theta+R_t w. \tag{13}$$

$$p_s\sigma\phi=\Delta\phi-\xi^2\phi+R_c f(z)w. \tag{14}$$

To proceed further we then take *curlcurl* of (12), and retain the third component of the resulting equation, namely

$$0=-\Delta w+R_t g(z)\Delta^*\theta-R_c g(z)\Delta^*\phi-M^2D^2 w, \tag{15}$$

where $\Delta^*=\partial^2/\partial x^2+\partial^2/\partial y^2$ and $D=d/dz$.

Next, due to the periodicity of the solution in the (x, y) variables we may write w and ϕ as

$$w=W(z)h(x, y),\ \theta=\Theta(z)h(x, y) \text{ and } \phi=\Phi(z)h(x, y),$$

where h is a plane-tiling planform so that

$$\Delta^* h=-a^2 h, \tag{16}$$

where a is the wavenumber. Such planforms are discussed in detail in [45], p.43-52 and [32], p.51. Eqs. (13)-(15) reduce to

$$((1+M^2)D^2-a^2)W+R_t g(z)a^2\Theta-R_c g(z)a^2\Phi=0, \quad (17)$$

$$(D^2-a^2)\Theta+R_t W=p_r\sigma\Theta. \quad (18)$$

$$(D^2-a^2)\Phi-\xi^2\Phi+R_c f(z)W=p_s\sigma\Phi. \quad (19)$$

The boundary conditions we employ herein are those appropriate to two fixed surfaces and so

$$W=\Theta=\Phi=0, \text{ on } z=0, 1. \quad (20)$$

System (17)-(20) represents an eigenvalue problem for the eigenvalues σ with parameters a, M, ξ, η, p_r, p_s, R_t and R_c.

When adopting a linear analysis approach, the perturbation to the steady state is assumed to be small, and so nonlinear terms in the governing set of partial differential equations are discarded. It has been proved that linear analysis often provides little information on the behavior of the nonlinear system [32], so in such cases only instability can be deduced from the linear thresholds, as any potential growth in the nonlinear terms is not considered.

To develop a nonlinear energy stability analysis, let V be a period cell for the disturbance solution in Eqs. (7)-(10). Let $\|\cdot\|$ and $(\cdot, \cdot)$ be the norm and inner product on the Hilbert space $L^2(V)$. We multiply Eq. (7) by u_i and integrate over V. After some integrations by parts, use of the boundary conditions (11), and employing Eq. (8) we derive the identity

$$0=-\|\mathbf{u}\|^2+R(w, g\theta)-R_c(w, g\phi)-M^2(\|\mathbf{u}\|^2-\|w\|^2). \quad (21)$$

Next, multiply Eqs. (9) and (10) by θ and ϕ, then integrate over V, to see that after further integrations by parts and use of (8) and (11), we obtain

$$\frac{p_r}{2}\frac{d}{dt}\|\theta\|^2=R(fw, \theta)-\|\nabla\theta\|^2. \quad (22)$$

$$\frac{p_s}{2}\frac{d}{dt}\|\phi\|^2=R_c(fw, \phi)-\xi^2\|\phi\|^2-\|\nabla\phi\|^2. \quad (23)$$

The idea is to now add (21) + λ_1 (22) + λ_2 (23) for positive parameters λ_1 and λ_2 which we later select optimally. This leads to the energy equation

$$\frac{dE}{dt}=I-D, \quad (24)$$

where E, I and D are defined by

$$E(t)=p_r\frac{\lambda_1}{2}\|\theta\|^2+p_s\frac{\lambda_2}{2}\|\phi\|^2,$$
$$I=R_t(w, \theta[g+\lambda_1])-R_c(w, \phi[g-\lambda_2 f]), \quad (25)$$
$$D=\|\mathbf{u}\|^2+\lambda_1\|\nabla\theta\|^2+\lambda_2\|\nabla\phi\|^2+\lambda_2\xi^2\|\phi\|^2+M^2(\|\mathbf{u}\|^2+\|v\|^2),$$

where **u** is explicitly written as **u**=(u, v, w). Define now

$$\frac{1}{R_E}=\max_H\frac{I}{D}, \quad (26)$$

where H is the space of admissible solutions and then from (24) we find

$$\frac{dE}{dt}\le-D\left(1-\frac{1}{R_E}\right), \quad (27)$$

If $R_E>1$ then with χ_1 being the constant in poincare's inequality, it follows that $D>cE$ where $c=\min\{2(\chi_1+\xi^2)p_s^{-1}, 2\chi_1 p_r^{-1}\}$. Hence it follows that

$$\frac{dE}{dt}\le-cE\left(\frac{R_E-1}{R_E}\right).$$

Thus, letting $\varepsilon=c(R_E-1)/R_E$ we have $E(t)\le E(0)e^{-\varepsilon t}$ which tends to 0 as $t\to\infty$, so we have shown the decay of ϕ, θ and u.

The Euler-Lagrange equations which arise from (26) are:

$$-2u_i+R_t k_i(g+\lambda_1)\theta-R_c k_i(g-\lambda_2 f)\phi-2M^2(u_i-k_i w)=\zeta_{,i}, \quad (28)$$

$$2\lambda_1\Delta\theta+R_t(g+\lambda_1)w=0, \quad (29)$$

$$2\lambda_2\Delta\phi-2\lambda_2\xi^2\phi-R_c(g-\lambda_2 f)w=0, \quad (30)$$

where ζ is a lagrange multiplier. To solve the energy eigenvalue problem (28)-(30) we remove the ζ term by taking *curlcurl* of (28) to arrive at the system

$$-2\Delta w-2M^2 w_{,zz}+R_t(g+\lambda_1)\Delta^*\theta-R_c(g-\lambda_2 f)\Delta^*\phi=0, \quad (31)$$

$$2\lambda_1\Delta\theta-R_t(g+\lambda_1)w=0. \quad (32)$$

$$2\lambda_2\Delta\phi-2\lambda_2\xi^2\phi-R_c(g-\lambda_2 f)w=0. \quad (33)$$

Again, the representations $w=W(z)h(x, y)$, $\theta=\Theta h(x, y)$ and $\phi=\Phi(z)h(x, y)$ are introduced and we solve (31)-(33) as

$$2(D^2-a^2)W+2M^2D^2W-a^2R_c(g-\lambda_2 f)\Phi=-a^2R_t(g+\lambda_1)\Theta, \quad (34)$$

$$2\lambda_1(D^2-a^2)\Theta=-R_t(g+\lambda_1)W, \quad (35)$$

$$2\lambda_2(D^2-a^2)\Phi-2\lambda_2\xi^2\Phi-R_c(g-\lambda_2 f)W=0, \quad (36)$$

together with boundary conditions (20). Numerical results are presented in the next section.

STABILITY ANALYSIS RESULTS

We approximate (17)-(19) using three different numerical techniques to ensure accuracy, namely Chebyshev collocation, finite elements and finite differences methods (cf. [46]). Then, we have solved the resulting system for eigenvalues σ_j by using the QZ algorithm from Matlab routines. Once the eigenvalues σ_j are found we use the secant method to locate where σ_j^R, $\sigma_j=\sigma_j^R+\sigma_j^I$ being the real and imaginary parts of eigenvalue σ_j. The value of R which makes $\sigma_1^R=0$, σ_1^R being the largest eigenvalue, is the critical value of R for a^2 fixed. We then use golden section search to minimize over a^2 and find the critical value of R^2 for linear instability.

Moreover, system (34)-(36) was approximated by using the same numerical methods which have been used for linear stability analysis. Then, we can determine the critical Rayleigh Ra_E for fixed a^2, λ_1 and λ_2. Next, we employ golden section search to minimize in a^2 and then maximize in λ_1 and λ_2 to determine Ra_E for nonlinear energy stability,

$$Ra_E=\max_{\lambda_1, \lambda_2}\min_{a^2}R_t^2(a^2, \lambda_1, \lambda_2), \quad (37)$$

where for all $R^2<Ra_E$ we have stability.

In our use of the Chebyshev collocation method, we used polynomial of degree between 20 and 30. Usually 25 was found to be

sufficient but convergence was checked by varying the degree by examining the convergence of the associated eigenvector (which yields the approximate associated eigenfunction). However, for finite elements, we have checked the convergence and found that convergence to eight decimal places was achieved with three elements with each element containing 11 nodes. For the finite difference scheme the convergence was tested and we found that convergence to eight decimal places was achieved with h=0.001.

The numerical results are presented for the gravity field g(z)= $1-\tilde{\varepsilon}z$, while the numerical routine is applicable to a wide variety of other fields. To investigate the possibility of a very widely varying gravity field (one which even changes sign) we choose $\tilde{\varepsilon}$ to vary from 0 to 1.5. Such fields are of interest in laboratory experiments in areas of crystal growth and other applications, although a plane layer would not be the geometry studied. Nevertheless, our results may help us to understand such situations. The results in this paper are given for $p_r=M_1=\hat{\varepsilon}=1$ and $p_s=5$.

If the layer is salted and heated from below, a linear instability analysis is more difficult because it includes an oscillatory convection. We found that the values of wave numbers for oscillatory convection are very close to the values of wave numbers for stationary convection; thus the computations of the critical Rayleigh numbers will be difficult, especially in the period around the intersection points.

Figs. 2, 3 and 4 give a visual representation of the linear instability and nonlinear stability thresholds with different strengths of the magnetic field. The remaining parameters are held fixed at $\tilde{\varepsilon}=0$, $\xi=1$ and $\eta=1$. These figures show the effect of increasing solute

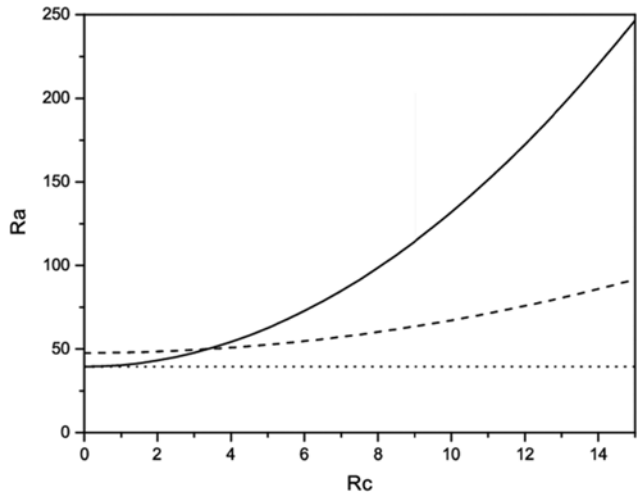

Fig. 2. Visual representation of stationary linear instability (solid line), oscillatory linear instability (dashed line) and nonlinear stability (dotted line) thresholds, with critical Rayleigh number plotted against R_c, where $M^2=0$, $\tilde{\varepsilon}=0$, $\xi=1$ and $\eta=1$.

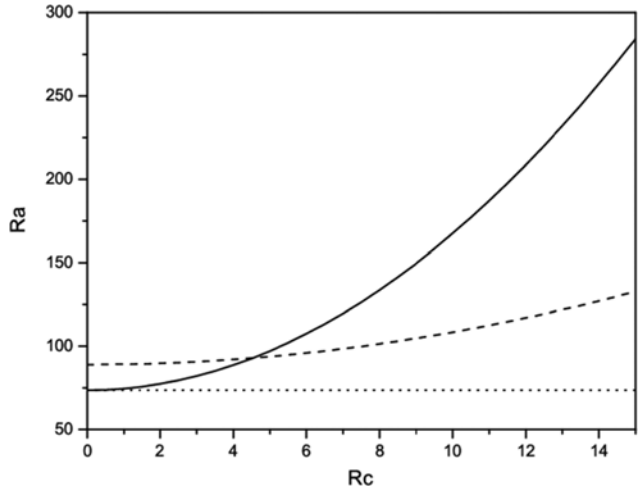

Fig. 3. Visual representation of stationary linear instability (solid line), oscillatory linear instability (dashed line) and nonlinear stability (dotted line) thresholds, with critical Rayleigh number plotted against R_c, where $M^2=2$, $\tilde{\varepsilon}=0$, $\xi=1$ and $\eta=1$.

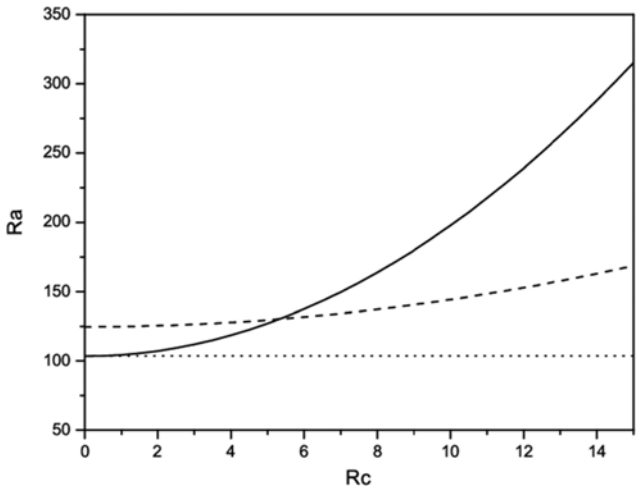

Fig. 4. Visual representation of stationary linear instability (solid line), oscillatory linear instability (dashed line) and nonlinear stability (dotted line) thresholds, with critical Rayleigh number plotted against R_c, where $M^2=4$, $\tilde{\varepsilon}=0$, $\xi=1$ and $\eta=1$.

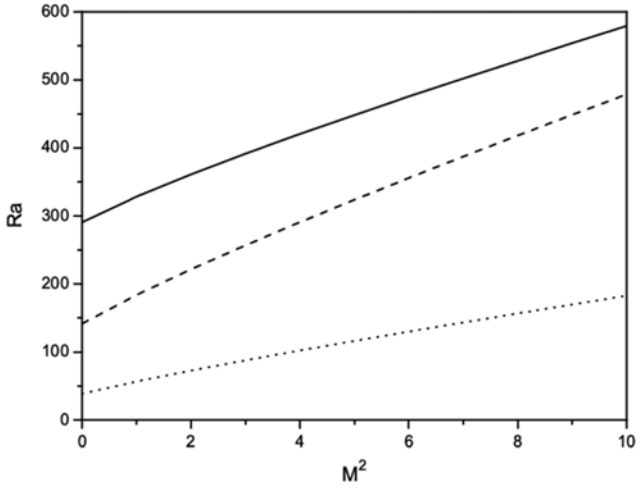

Fig. 5. Visual representation of stationary linear instability (solid line), oscillatory linear instability (dashed line) and nonlinear stability (dotted line) thresholds, with critical Rayleigh number plotted against M^2, where $R_c=15$, $\tilde{\varepsilon}=1$, $\xi=1$ and $\eta=1$.

Rayleigh number on the critical Rayleigh number for various values of M^2. It is clear that an increase in M^2 causes the system to become more stable, which we would physically expect. As R_c is increased, the oscillatory modes become present in the linear instability thresholds. This causes the correlation between the linear and nonlinear thresholds to substantially deteriorate. Fig. 5 demonstrates that Ra increases with increasing M^2, which shows the stabilizing effect of M^2. Note that the nonlinear stability curves are not close to those of linear theory. This shows that possible sub-critical instabilities may arise in a very large range of Rayleigh numbers, and it also demonstrates that linear instability theory does not correctly capture the physics of the onset of convection.

Figs. 6, 7 and 8 give a visual representation of the linear instability and nonlinear stability boundaries for a selection of gravity field strength. The remaining parameters are held fixed at $M^2=1$, $\xi=1$ and $\eta=1$. It is clear that Ra increases with increasing $\tilde{\varepsilon}$, which refers to the stabilizing effect of $\tilde{\varepsilon}$. Clearly, for small values of R_c the linear and nonlinear thresholds have substantial correlation, demonstrating the suitability of linear theory to predict the physics of the onset of convection. As the solute Rayleigh number increase, the thresholds have less correlation. An alternative energy analysis may have to be devised to improve threshold correlation. Also, Fig. 9 shows the stabilizing effect of $\tilde{\varepsilon}$ where the critical Rayleigh number increases with increasing gravity field strength.

Fig. 10 shows how increasing ξ corresponds, in general, to stabilization. This figure demonstrates quantitatively the stabilizing effect of the chemical reaction. Again, it is very noticeable that the nonlinear energy stability curves are not close to those of linear instability. This reinforces the fact that the linear curves are not a true representation that the physics of the onset of convection is being correctly reflected. The gap between the curves represents the large band where sub-critical bifurcation may possibly occur.

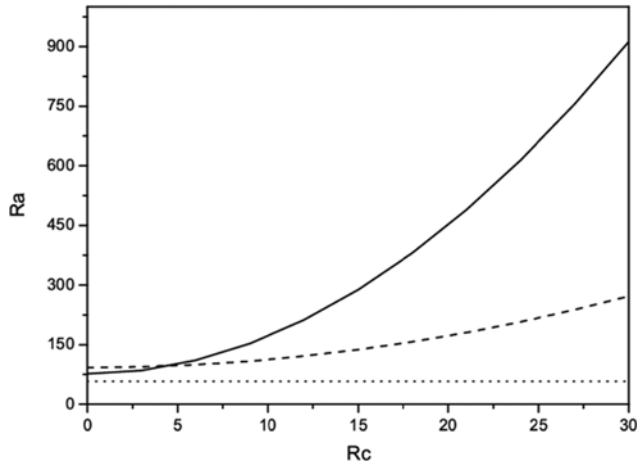

Fig. 6. Visual representation of stationary linear instability (solid line), oscillatory linear instability (dashed line) and nonlinear stability (dotted line) thresholds, with critical Rayleigh number plotted against R_c, where $M^2=1$, $\tilde{\varepsilon}=0.5$, $\xi=1$ and $\eta=1$.

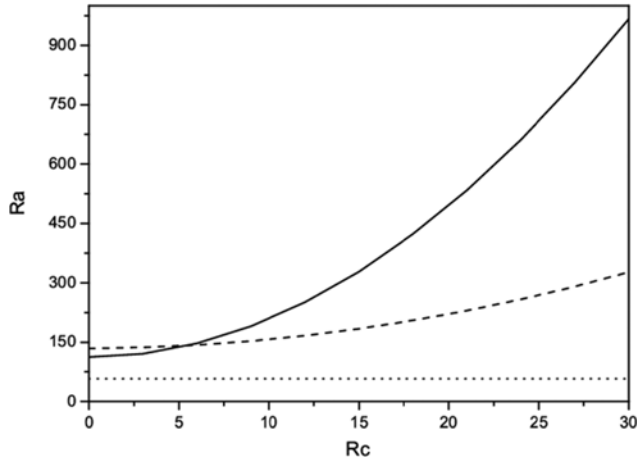

Fig. 7. Visual representation of stationary linear instability (solid line), oscillatory linear instability (dashed line) and nonlinear stability (dotted line) thresholds, with critical Rayleigh number plotted against R_c, where $M^2=1$, $\tilde{\varepsilon}=1$, $\xi=1$ and $\eta=1$.

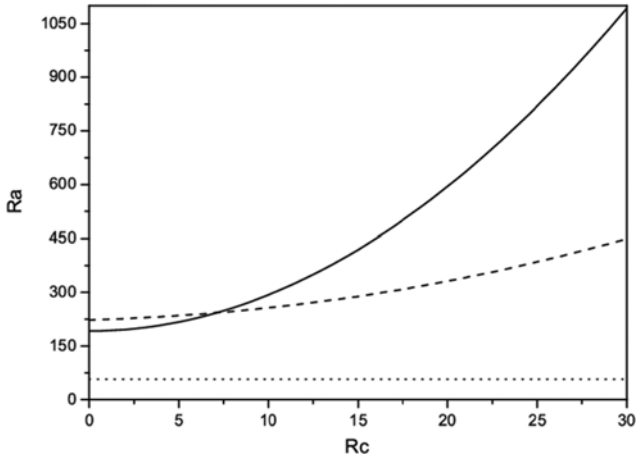

Fig. 8. Visual representation of stationary linear instability (solid line), oscillatory linear instability (dashed line) and nonlinear stability (dotted line) thresholds, with critical Rayleigh number plotted against R_c, where $M^2=1$, $\tilde{\varepsilon}=1.5$, $\xi=1$ and $\eta=1$.

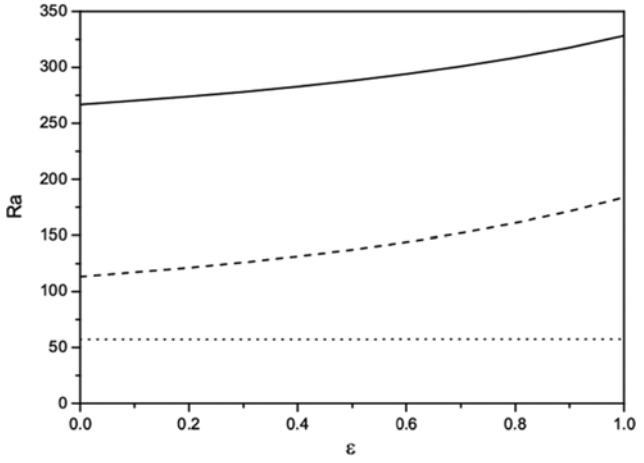

Fig. 9. Visual representation of stationary linear instability (solid line), oscillatory linear instability (dashed line) and nonlinear stability (dotted line) thresholds, with critical Rayleigh number plotted against $\tilde{\varepsilon}$, where $R_c=15$, $M^2=1$, $\xi=1$ and $\eta=1$.

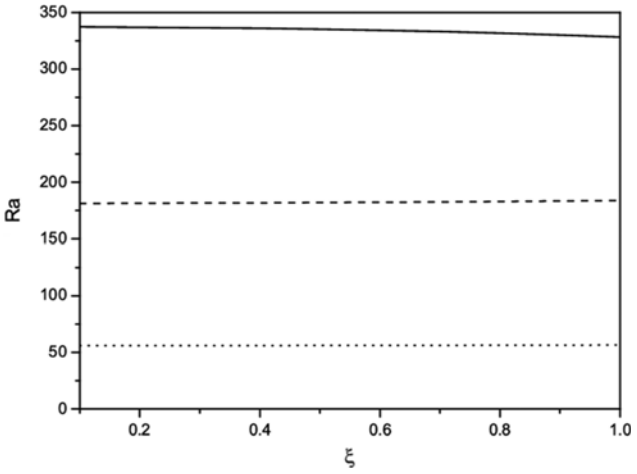

Fig. 10. Visual representation of stationary linear instability (solid line), oscillatory linear instability (dashed line) and nonlinear stability (dotted line) thresholds, with critical Rayleigh number plotted against ξ, where R_c=15, $\tilde{\varepsilon}$=1, M^2=1 and η=1.

THREE-DIMENSIONAL SIMULATIONS

We now develop a three-dimensional approach to solve the time-dependent governing Eqs. (1)-(4) to assess the accuracy of the linear instability and nonlinear stability thresholds.

In this paper, we present an efficient, stable, and accurate finite difference scheme for computing the convective motion of an incompressible fluid in a porous solid. The emphasis is on three dimensions and nonstaggered grids. We introduce a second-order accurate method based on the **u**−curl(**u**) formulation on the nonstaggered grid whose performance on uniform grids is comparable with the finite scheme. We will pay special attention to how accurately the divergence-free conditions for **u** and curl(**u**) are satisfied.

By using the curl operator in Eq. (7), one gets the following dimensionless form of the transport equation:

$$\omega = R_t \nabla \times g(z)\theta \mathbf{k} - R_c \nabla \times g(z)\phi \mathbf{k} - M^2 \omega + M^2 \nabla \times w\mathbf{k}, \tag{38}$$

where the vector $w=(\zeta_1, \zeta_2, \zeta_3)$ is defined as

$$\omega = \nabla \times \mathbf{u}. \tag{39}$$

To calculate **u** from ω, it is convenient to introduce a vector $\psi=(\psi_1, \psi_2, \psi_3)$ which may be looked upon as the three-dimensional counterpart of two-dimensional stream function. The vector potential is defined by

$$\mathbf{u} = \nabla \times \psi. \tag{40}$$

It easy to show the existence of such a vector potential for a solenoidal vector field ($\nabla \cdot \mathbf{u} = 0$). Such a vector potential can be required to be solenoidal, i.e.,

$$\nabla \cdot \psi = 0. \tag{41}$$

Substituting Eq. (40) in Eq. (39) and using Eq. (41) yields

$$\nabla^2 \psi = -\omega. \tag{42}$$

The set of Eqs. (9), (10), (38), (40) and (42) with appropriate boundary conditions were found to be a convenient form for numerical computations. The discretized form of these equations using second-order finite difference scheme can be written as:

$$(\delta_x^2 + \delta_y^2 + \delta_z^2)\psi_{1i,j,k}^{n+1} = -\zeta_{1i,j,k}^{n+1},\ i, j, k=1, \ldots, m-1, \tag{43}$$

$$(\delta_x^2 + \delta_y^2 + \delta_z^2)\psi_{2i,j,k}^{n+1} = -\zeta_{2i,j,k}^{n+1},\ i, j, k=1, \ldots, m-1, \tag{44}$$

$$(\delta_x^2 + \delta_y^2 + \delta_z^2)\psi_{3i,j,k}^{n+1} = -\zeta_{3i,j,k}^{n+1},\ i, j, k=1, \ldots, m-1. \tag{45}$$

$$u_{i,j,k}^{n+1} = \delta_y \psi_{3i,j,k}^{n+1} - \delta_z \psi_{2i,j,k}^{n+1},\ i, j, k=1, \ldots, m-1, \tag{46}$$

$$v_{i,j,k}^{n+1} = \delta_z \psi_{1i,j,k}^{n+1} - \delta_x \psi_{3i,j,k}^{n+1},\ i, j, k=1, \ldots, m-1, \tag{47}$$

$$u_{i,j,k}^{n+1} = \delta_x \psi_{2i,j,k}^{n+1} - \delta_y \psi_{1i,j,k}^{n+1},\ i, j, k=1, \ldots, m-1, \tag{48}$$

$$(1+M^2)\zeta_{1i,j,k}^{n+1} = g(z_k)(R_t \delta_y \theta_{i,j,k}^{n+1} - R_c \delta_y \phi_{i,j,k}^{n+1}) + M^2 \delta_y w_{i,j,k}^{n+1},$$
$$i, j, k=1, \ldots, m-1, \tag{49}$$

$$(1+M^2)\zeta_{2i,j,k}^{n+1} = g(z_k)(R_c \delta_x \phi_{i,j,k}^{n+1} - R_t \delta_x \theta_{i,j,k}^{n+1}) + M^2 \delta_x w_{i,j,k}^{n+1},$$
$$i, j, k=1, \ldots, m-1, \tag{50}$$

$$\zeta_{3i,j,k}^{n+1} = 0,\ i, j, k=1, \ldots, m-1, \tag{51}$$

$$p_r\left(\frac{\theta_{i,j,k}^{n+1} - \theta_{i,j,k}^{n}}{\Delta t} + M_1 u_{i,j,k}^{n} \delta_x \theta_{i,j,k}^{n} + M_1 v_{i,j,k}^{n} \delta_y \theta_{i,j,k}^{n} + M_1 w_{i,j,k}^{n} \delta_z \theta_{i,j,k}^{n}\right) = R_t w_{i,j,k}^{n} + (\delta_x^2 + \delta_y^2 + \delta_z^2)\theta_{i,j,k}^{n},$$
$$i, j, k=1, \ldots, m-1, \tag{52}$$

$$p_s\left(\frac{\phi_{i,j,k}^{n+1} - \phi_{i,j,k}^{n}}{\Delta t} + \hat{\varepsilon} u_{i,j,k}^{n} \delta_x \phi_{i,j,k}^{n} + \hat{\varepsilon} v_{i,j,k}^{n} \delta_y \phi_{i,j,k}^{n} + \hat{\varepsilon} w_{i,j,k}^{n} \delta_z \phi_{i,j,k}^{n}\right) = R_c f(z_k) w_{i,j,k}^{n} + (\delta_x^2 + \delta_y^2 + \delta_z^2)\phi_{i,j,k}^{n} - \xi^2 \phi_{i,j,k}^{n},$$
$$i, j, k=1, \ldots, m-1, \tag{53}$$

where δ_x^2, δ_y^2, δ_z^2 are the second-order central difference operators, and δ_x, δ_y, δ_z are the first-order central difference operators. Here, u_{ijk}^{n+1}, v_{ijk}^{n+1}, w_{ijk}^{n+1}, ζ_{3ijk}^{n+1}, θ_{ijk}^{n+1} and ϕ_{ijk}^{n+1}, are computed explicitly from (46), (47), (48), (51), (52) and (53), respectively, while $\psi_{1i,j,k}^{n+1}$, $\psi_{2i,j,k}^{n+1}$, $\psi_{3i,j,k}^{n+1}$, ζ_{1ijk}^{n+1}, and ζ_{2ijk}^{n+1} are computed from (43), (44), (45), (49), and (50), respectively, implicitly using the Gauss-Seidel iteration method. The temperature and concentration on the boundary can be computed explicitly using (11).

Note that our scheme is flexible for various Ra values, and thus the grid resolution has been selected according to the Ra values. We decrease the values of Δx, Δy and Δz as the value of Ra increases. However, for this problem, Δx=Δy=Δz=0.02 is enough to give us very accurate results.

NUMERICAL RESULTS

IIn this section, Ra_L, is the critical Rayleigh number for linear instability theory and Ra_E is the critical Rayleigh number for the global nonlinear stability theory. The corresponding critical wavenumbers of the linear instability will be denoted by a_L. Table 1 presents the numerical results of the linear instability and non-linear stability analyses. The dimensions of the box, which are calculated according to the critical wavenumber, are shown in Table 1. In this table Lx and Ly are box dimensions in the x and y directions, respectively. The box dimension in the z direction is always equal to 1. We assume that the perturbation fields (u, θ, ϕ, P) are periodic in

Table 1. Critical Rayleigh and wavenumbers of the linear instability and nonlinear stability theories for $\tilde{\varepsilon}$=1.5, M^2=1, ξ=1 and η=1

R_c	Ra_L	a_L^2	Ra_E	a_E^2	λ_1	λ_2	Lx	Ly
3	201.1400	17.4000	57.3100	14.0000	1.0200	0.31	2.3	2
7	241.5700	17.0500	57.3100	14.1600	1.0200	0.32	2.2	2.1
7.5	244.7600	16.8900	57.3100	14.1600	1.0200	0.32	2.9	1.8
12	268.5300	17.7400	57.3100	14.5900	1.0200	0.31	2.4	1.9
20	331.6500	18.4200	57.3100	15.8800	1.0200	0.31	2.5	1.8
30	449.6100	19.0000	57.3100	17.8900	1.0200	0.31	2.2	1.9

the x and y directions and denoted by $\Omega=[0, 2\pi/a_x]\times[0, 2\pi/a_y]\times[0, 1]$ to be the periodicity cell, where a_x and a_y are the wavenumbers in the x and y directions, respectively. a_x and a_y are evaluated according to the critical wavenumbers a_L where $a_L^2=a_x^2+a_y^2$, where $Lx=2\pi/a_x$ and $Ly=2\pi/a_y$. The values of Lx and Ly in Table 1 may be rearranged to yield a number of possible solutions for each value of the critical wavenumbers. However, we select a solution so that these two values are similar to avoid any possible stabilisation effect from walls.

For numerical solutions in three dimensions, we used $\Delta t=5\times10^{-5}$ and $\Delta x=\Delta y=\Delta z=0.02$. The convergence criterion was selected to make sure that the solutions arrive at a steady state. The convergence criterion is

$$\chi=\max_{i,j,k}\{|\zeta_{1i,j,k}^{n+1}-\zeta_{1i,j,k}^{n}|, |\zeta_{2i,j,k}^{n+1}-\zeta_{2i,j,k}^{n}|, |\zeta_{3i,j,k}^{n+1}-\zeta_{3i,j,k}^{n}|, |\theta_{i,j,k}^{n+1}-\theta_{i,j,k}^{n}|, |\phi_{i,j,k}^{n+1}-\phi_{i,j,k}^{n}|\},$$

and we select $\chi=10^{-6}$. The program will continue computing the results for new time steps until the results satisfy the convergence criterion. Otherwise, if the solution cannot arrive at any steady state and oscillate, we present the results at τ=6.

To solve Eqs. (43)-(45) using the Gauss-Seidel iteration method, in the first time step we give an initial value to the potential vector and we denote $\psi_{1ijk}^{1,k}$, $\psi_{2ijk}^{1,k}$, $\psi_{3ijk}^{1,k}$ to be the potential vector. Then, using these initial values, we compute new values which we denote by $\psi_{1ijk}^{1,k+1}$, $\psi_{2ijk}^{1,k+1}$ $\psi_{3ijk}^{1,k+1}$ and use these values to evaluate new values. The program will continue in this process until the convergence criterion is satisfied:

$$\eta=\max_{i,j,k}\{|\psi_{1ijk}^{1,k+1}-\psi_{1ijk}^{1,k}|, |\psi_{2ijk}^{1,k+1}-\psi_{2ijk}^{1,k}|, |\psi_{3ijk}^{1,k+1}-\psi_{3ijk}^{1,k}|\}<10^{-5}.$$

In the next time steps, the values of ψ_{1ijk}, ψ_{2ijk}, ψ_{3ijk} in the time step n will be the initial values to the next time step.

To display the numerical results clearly, the temperature, concentration, velocity and vorticity contours are plotted in Figs. 11-17 at τ=6, $\tilde{\varepsilon}$=1.5, M^2=1, ξ=1, R_c=7.5, η=1 and Ra=227 with mesh size of 146×91×51. In these figures, the temperature, concentra-

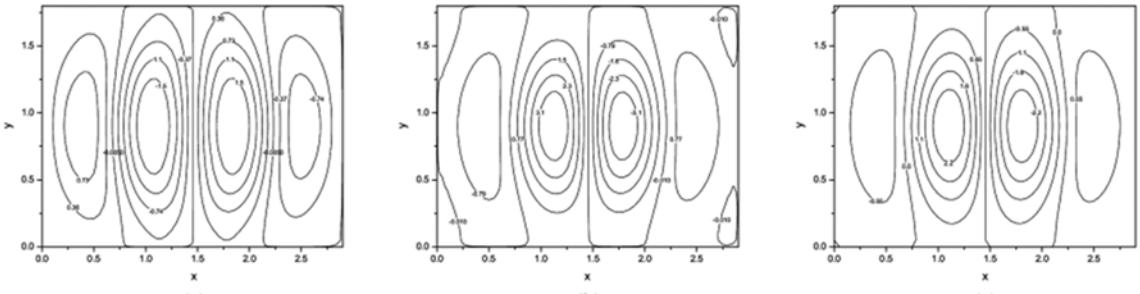

Fig. 11. Contour plot of u, (a) z=0.25, (b) z=0.5, (c) z=0.75.

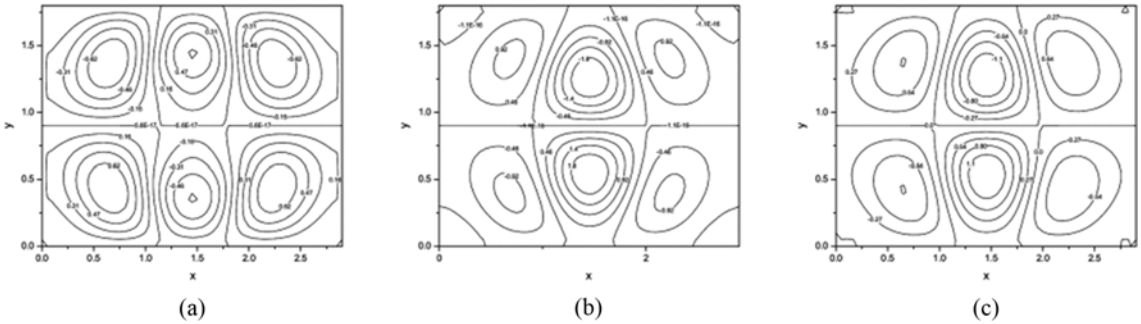

Fig. 12. Contour plot of v, (a) z=0.25, (b) z=0.5, (c) z=0.75.

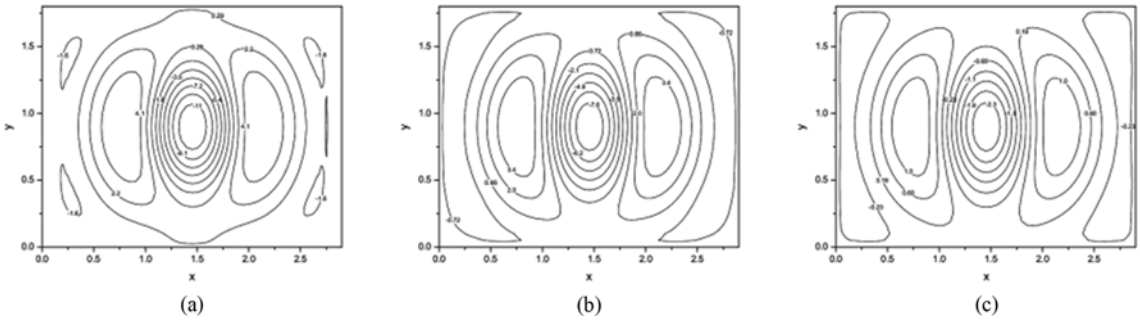

Fig. 13. Contour plot of w, (a) z=0.25, (b) z=0.5, (c) z=0.75.

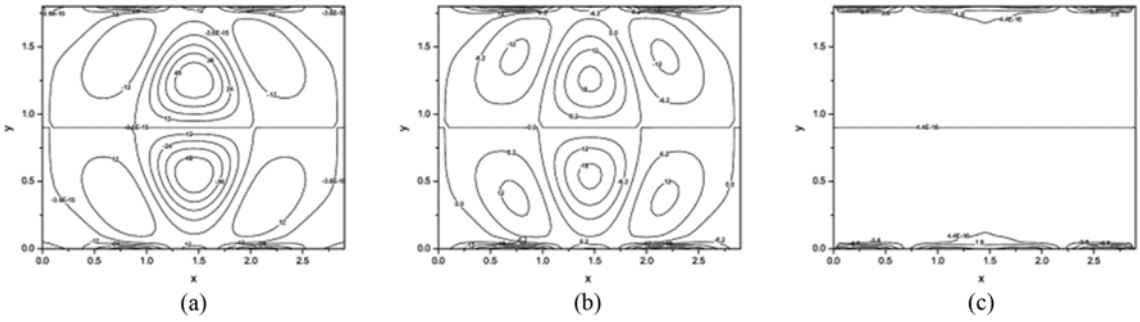

Fig. 14. Contour plot of ζ_1, (a) z=0.25, (b) z=0.5, (c) z=0.75.

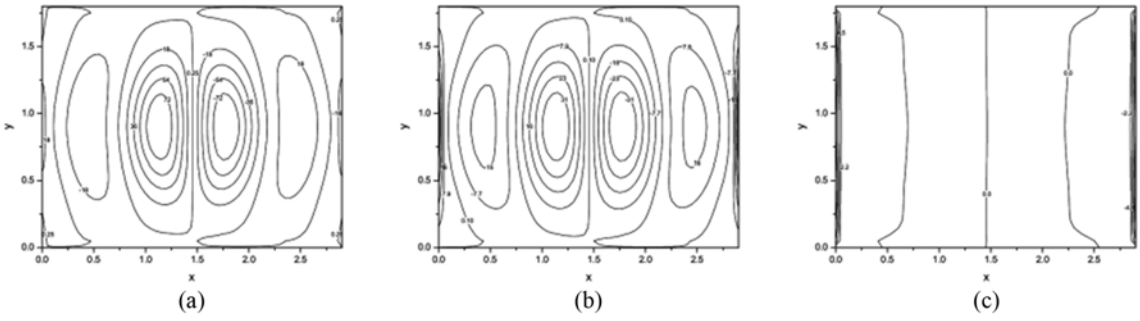

Fig. 15. Contour plot of ζ_2, (a) z=0.25, (b) z=0.5, (c) z=0.75.

tion, velocity and vorticity contours are presented at the time level τ=6 as the possibility of arriving the solution to any steady state is impossible. Figs. 11, 12, 13, 14, 15, 16 and 17 show the contours of u, v, w, ζ_1, ζ_2, θ and ϕ, respectively, at z=0.25, z=0.5 and z=0.75.

From Fig. 11, four recirculation cells are formulated and this may be attributed to finding the porous media which resist the obtained single cell. The side two cells (left and right) are similar in size and intensity but different in the rotating direction (clockwise CW and counterclockwise CCW), while the middle two cells also are similar in size and intensity but differ in rotating direction. The middle cells have maximum intensity of u of 1.5, 3.1 and 2.2 at z=0.25, 0.5 and 0.75 respectively.

Fig. 12 indicates the contour of perturbation velocity v at three locations, z=0.25, 0.5 and 0.75. There are six cells different in rotating direction that have a mirror images about horizontal and vertical mid lines of plane x−y. The periodic boundary conditions in the x and y directions make the rotating cells symmetric about horizontal and vertical mid lines in the x−y plane. The maximum intensity of v at z=0.5 in the opposite middle cells v_{max}=1.8 CW and CCW.

The velocity w presents the main velocity because the temperature difference between the lower and upper boundary $T_L>T_U$ makes the buoyancy effect (Boussinesq approximation) in the z-direction; also the concentration difference between the lower and upper boundary $C_L>C_U$ makes the mass diffusion in the z-direction. Fig. 13 clears the contour of w at z=0.25, 0.5 and 0.75. From Fig. 13, the maximum perturbation velocity in the three directions x, y and z isw, where the w_{max}=7.6 CW (negative sign), and there is symmetry about the mid vertical line because of the periodic conditions in the x-direction.

The vorticity distribution ζ_1 in x−y plane is presented in Fig. 14. The number of rotating cells is six at each location (z=0.25, 0.5 and 0.75). The cells in the upper half are rotated inverse the lower half; also the intensity of ζ_1 is graduated from local z=0.25 to z=0.75

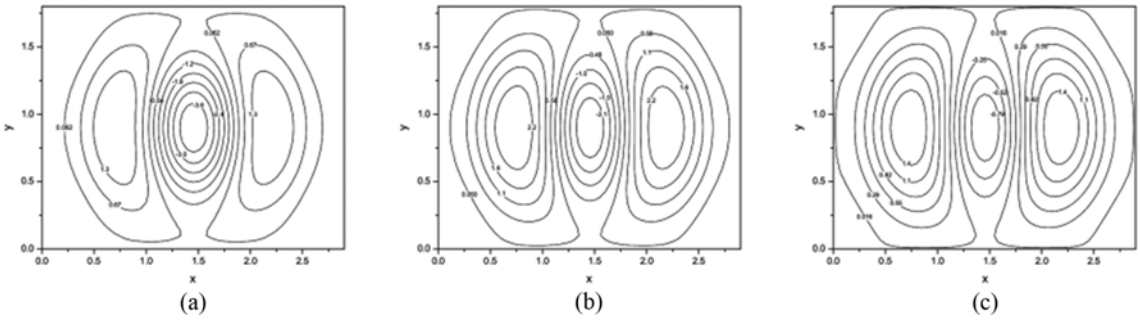

Fig. 16. Contour plot of θ, (a) z=0.25, (b) z=0.5, (c) z=0.75.

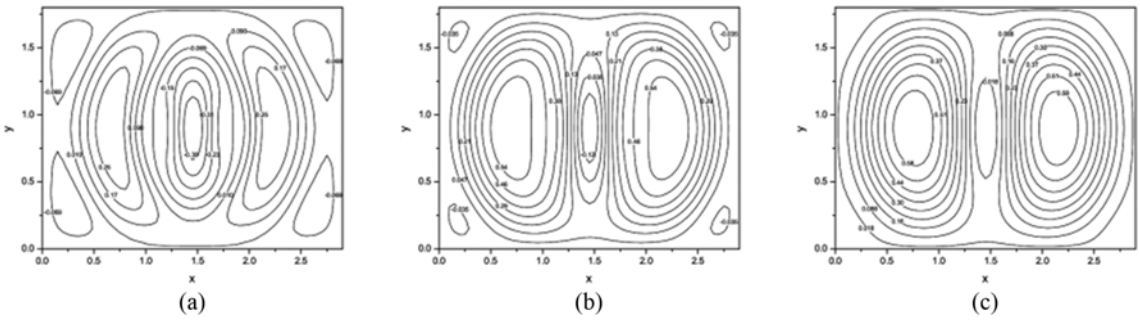

Fig. 17. Contour plot of θ, (a) z=0.25, (b) z=0.5, (c) z=0.75.

and maximum value at z=0.25 (ζ_{1max}=48, ζ_{1max}=18 and ζ_{1max}=5.7 at z=0.25, 0.5 and 0.75 respectively). This may be attributed to nearing the boundary layer obtained from diffusion of energy and concentration. Fig. 15 plots the contour of ζ_2 in the x−y plane. The number of rotating cells is four cells in the location z=0.25 and z=0.5 with two directions CW and CCW, and the cells are flattening vertically, except at z=0.75, where the value of ζ_2 becomes minimum, and the cells are diminished at the left and right sides, because far away from bottom plane of z. The maximum intensity of ζ_2 at z=0.25, 0.5 and 0.75 is 72, 31 and 4.5 respectively.

The perturbation of temperature θ is shown in Fig. 16, which shows that the magnitude of θ is graduated from z=0.25 to 0.75,

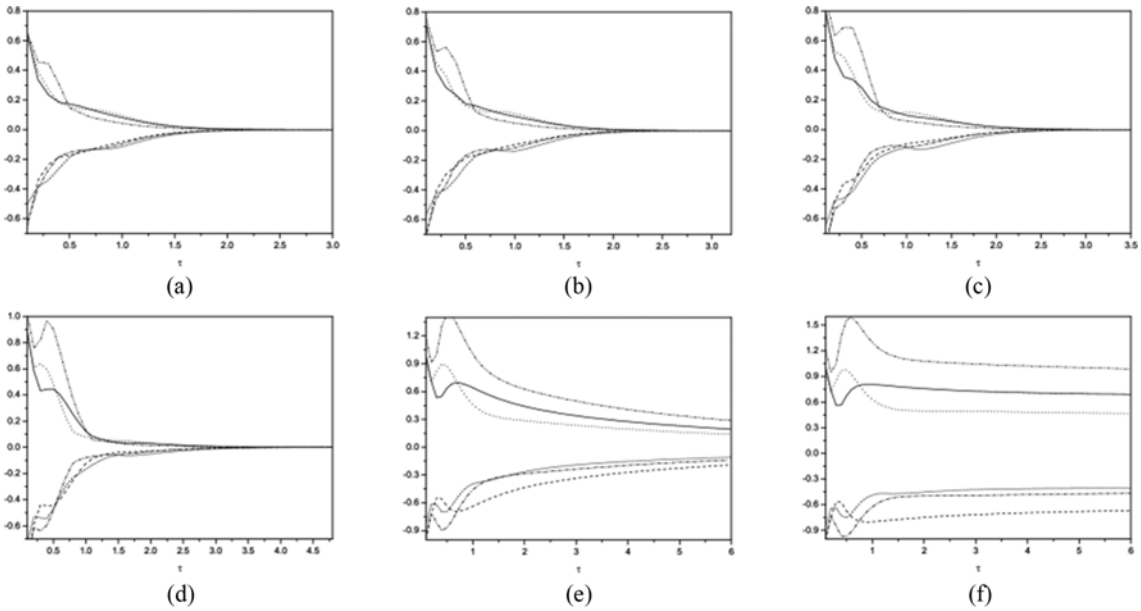

Fig. 18. The numerical results for different Ra. We present the results for the maximum and minimum values of velocities versus time for R_c=3, Ra_L=201.14, Ra_E=57.31, Lx=2.3, Ly=2. The solid, dash, dot, dash dot, dash dot dot and short dash lines represent u_{max}, u_{min}, v_{max}, v_{min}, w_{max}, and w_{min}, respectively. (a) Ra=158, (b) Ra=167, (c) Ra=176, (d) Ra=185, (e) Ra=194, (f) Ra=195.

where the boundary conditions are $T=T_L$ at z=0.25 and $T=T_U$ at z=0.75 ($T_L>T_U$). There are three cells that have different sign (positive and negative), and the side cells (left and right) have the same size, intensity and sign.

Fig. 17 plots the contour of ϕ at three positions: z=0.25, z=0.5 and z=0.75. The figure shows two big cells in the sides (right and left) and a single small cell in the middle which flattens vertically. Also, Fig. 17(b), (c) indicates two identical cells of perturbation of concentration ϕ, having the same the sign (positive sign) and magnitude. The maximum magnitude of ϕ of the side cells is 0.25, 0.54 and 0.58 at z=0.25, 0.5 and 0.75 respectively.

Figs. 18-23 show a summary of the numerical results where the maximum and minimum values of velocities versus time with $\tilde{\varepsilon}$= 1.5, M^2=1, ξ=1 and η=1 are presented. In Figs. 18 and 19 R_c=3 and R_c=7, respectively, were chosen, and for these cases the critical spectrum σ is found numerically to be always real. In Fig. 18, R_c=3 was selected, then, according to the stability analysis Ra_L= 201.14, Ra_E=57.31, Lx=2.3 and Ly=2 are obtained. Here, there is

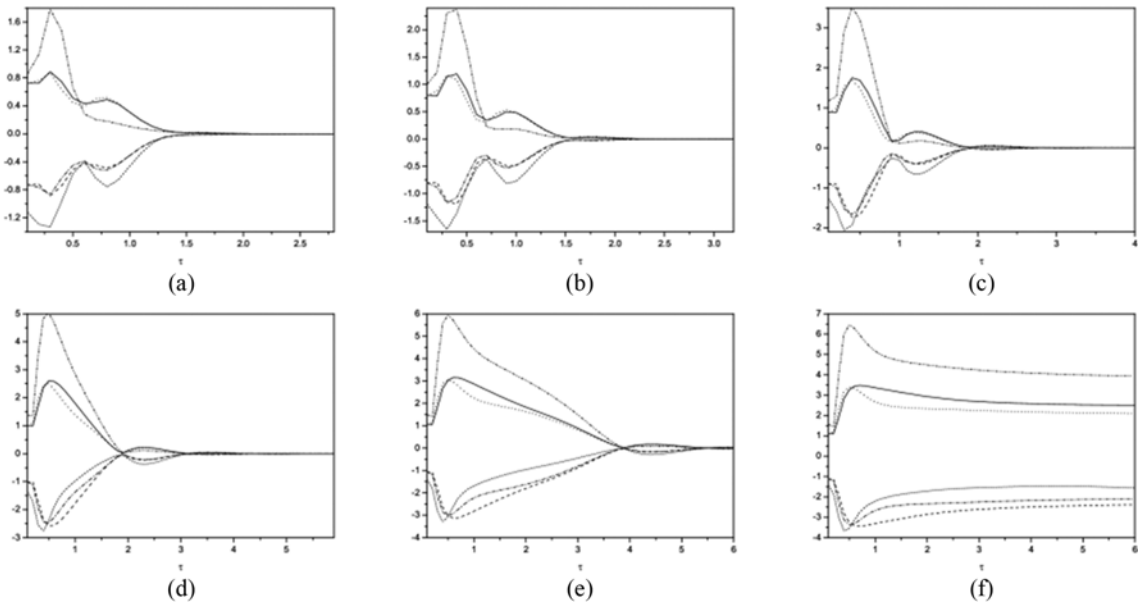

Fig. 19. The numerical results for different Ra. We present the results for the maximum and minimum values of velocities versus time for R_c=7, Ra_L=241.57, Ra_E=57.31, Lx=2.2, Ly=2.1. The solid, dash, dot, dash dot, dash dot dot and short dash lines represent u_{max}, u_{min}, v_{max}, v_{min}, w_{max}, and w_{min}, respectively. (a) Ra=194, (b) Ra=202, (c) Ra=211, (d) Ra=220, (e) Ra=224, (f) Ra=227.

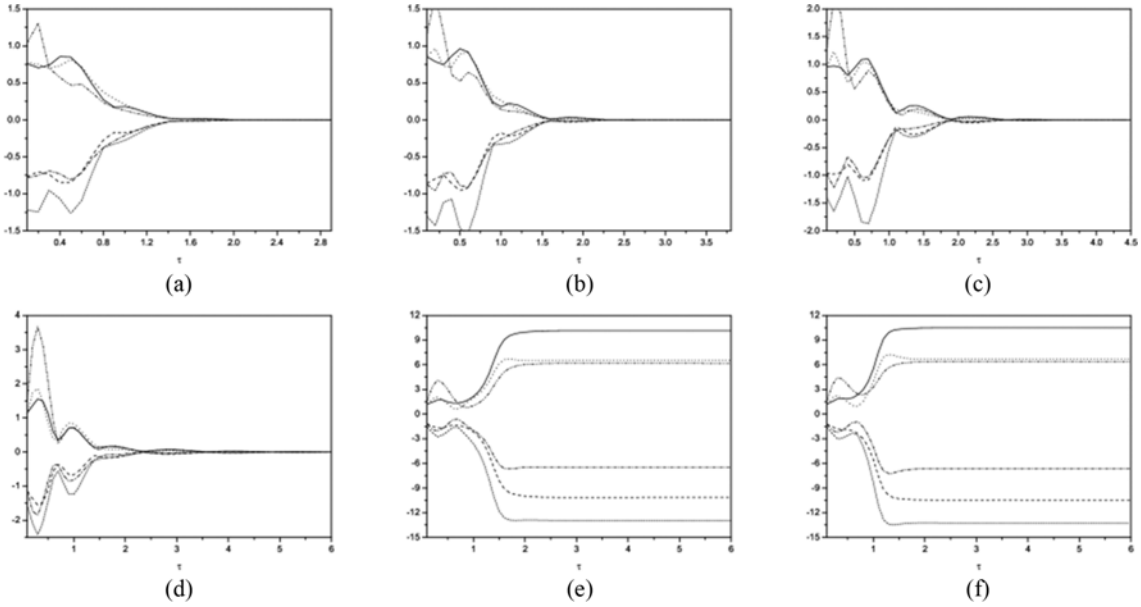

Fig. 20. The numerical results for different Ra. We present the results for the maximum and minimum values of velocities versus time for R_c=7.5, Ra_L=244.76, Ra_E=57.31, Lx=2.9, Ly=1.8. The solid, dash, dot, dash dot, dash dot dot and short dash lines represent u_{max}, u_{min}, v_{max}, v_{min}, w_{max}, and w_{min}, respectively. (a) Ra=194, (b) Ra=202, (c) Ra=211, (d) Ra=224, (e) Ra=227, (f) Ra=229.

clearly a very large subcritical stability region as there is a big difference between the critical Rayleigh numbers of linear and nonlinear theories. From Fig. 18, for Ra=158, the solutions satisfy the convergence criterion at τ=3.0553 and thus the solution arrives at the basic steady state within a short time. However, for Ra=167, Ra=176 and Ra=185, the program needs τ=3.20585, τ=3.5958 and τ=4.84635 respectively, to arrive at the basic steady state, which is expected as the required time to arrive at a steady state increases with increasing Ra values until the solution does not arrive at any steady state. Finally, for Ra=194 and Ra=195, the solutions do not arrive at any steady state and the program stops at τ=6. For Ra=194 and Ra=195, the program was allowed to run for a significant period to test the convection's long time behaviour. The values of the velocities increase at τ=8, and then decrease at τ=12 and continue in this oscillation. Here, according to the numerical results, the linear instability threshold is close to the actual threshold, i.e., the solutions reach the basic steady state before the linear instability threshold. The results in Fig. 19 indicate that the stability behavior is similar

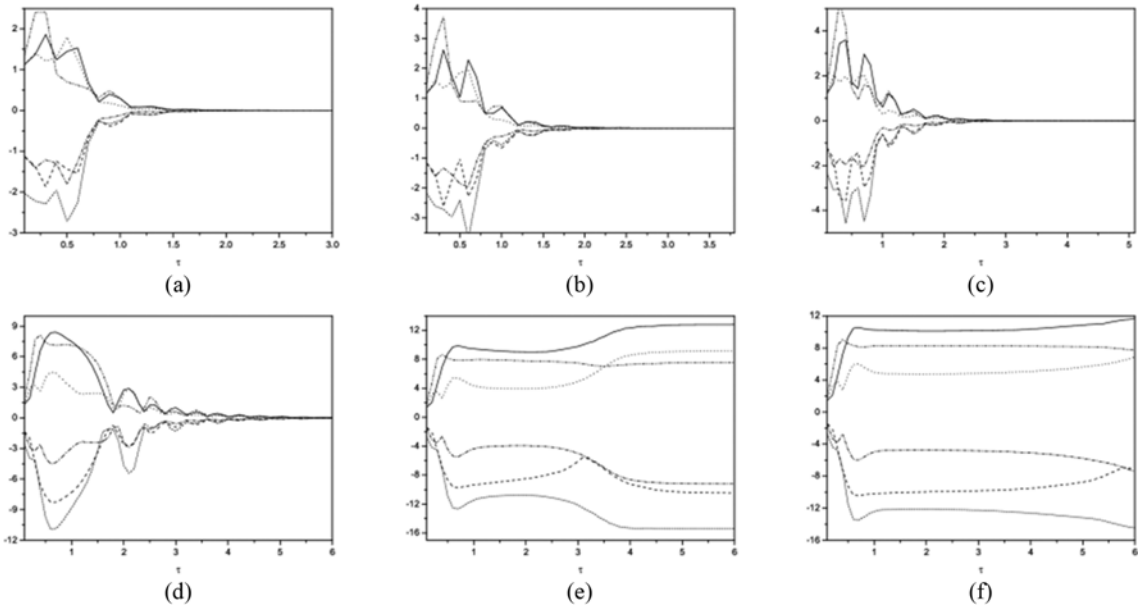

Fig. 21. The numerical results for different Ra. We present the results for the maximum and minimum values of velocities versus time for R_c=12, Ra_L=337.43, Ra_E=57.31, Lx=2.4, Ly=1.9. The solid, dash, dot, dash dot, dash dot dot and short dash lines represent u_{max}, u_{min}, v_{max}, v_{min}, w_{max}, and w_{min}, respectively. (a) Ra=229, (b) Ra=238, (c) Ra=246, (d) Ra=260, (e) Ra=262, (f) Ra=264.

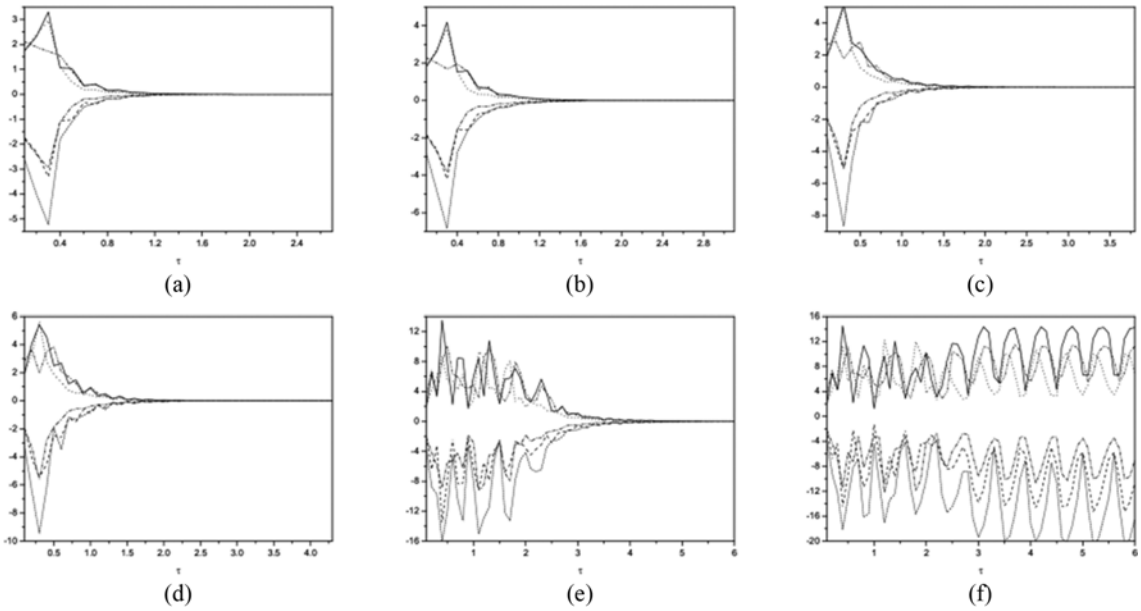

Fig. 22. The numerical results for different Ra. We present the results for the maximum and minimum values of velocities versus time for R_c=20, Ra_L=331.65, Ra_E=57.31, Lx=2.5, Ly=1.8. The solid, dash, dot, dash dot, dash dot dot and short dash lines represent u_{max}, u_{min}, v_{max}, v_{min}, w_{max}, and w_{min}, respectively. (a) Ra=290, (b) Ra=299, (c) Ra=308, (d) Ra=312, (e) Ra=327, (f) Ra=330.

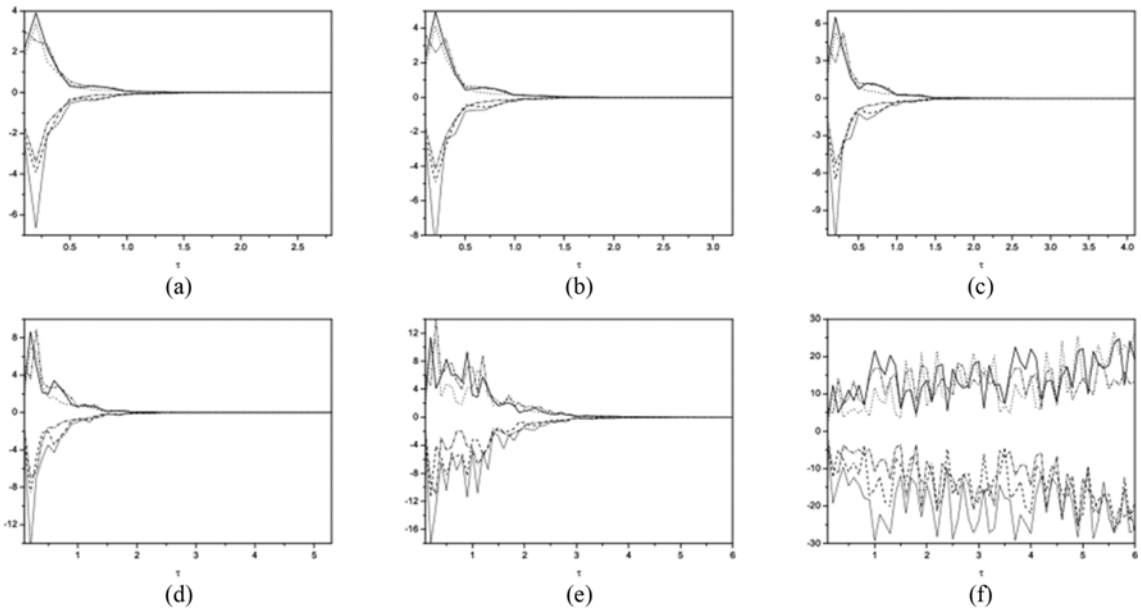

Fig. 23. The numerical results for different Ra. We present the results for the maximum and minimum values of velocities versus time for R_c=30, Ra_L=449.61, Ra_E=57.31, Lx=2.2, Ly=1.9. The solid, dash, dot, dash dot, dash dot dot and short dash lines represent u_{max}, u_{min}, v_{max}, v_{min}, w_{max}, and w_{min}, respectively. (a) Ra=414, (b) Ra=422, (c) Ra=431, (d) Ra=440, (e) Ra=449, (f) Ra=451.

to the stability behavior of Fig. 18, as it was found that the actual threshold was close to the linear instability threshold. However, in Fig. 19, R_c=7 and thus the value of R_c is very close to the switching point of convection from steady to oscillatory. In this case, the actual threshold will move slightly from the linear instability threshold.

At R_c=7.5, the nature of convection changes to oscillatory convection. For R_c=7.5 and R_c=12, the results are presented in Figs. 20 and 21, respectively, and in these cases, the numerical value of the critical spectrum σ is always complex. In Fig. 20, critical Rayleigh numbers for R_c=7.5 were computed; Eqs. (17)-(19) and (34)-(36) were solved, leading to the following stability results: Ra_L=244.76, Ra_E=57.31, Lx=2.9 and Ly=1.8. In this case, the difference between the critical Rayleigh numbers of linear and nonlinear theories is very large. Fig. 20 shows that for Ra=194, Ra=202 and Ra=211 the solutions reach the basic steady state and satisfy the convergence criterion at τ=2.94305, τ=3.8275 and τ=4.5548, respectively. Moreover, at R^2=224, the basic steady state at τ=6 could not be achieved, but there was a decrease in the solutions' values and therefore reaching a basic steady state at the next time levels is expected. Also, for Ra=227, and Ra=229, the solutions cannot achieve any steady state and the program stops at τ=6. For Ra=227, and Ra=229 the convection behavior oscillated and access to a stable state was impossible. For Fig. 21, R_c=12 was selected; then the R_c value moved from the switching point of convection from steady to oscillatory. The results of Fig. 20 demonstrate that the stability behavior is similar to the stability behavior of Fig. 21, as it was found that the actual threshold was close to the linear instability threshold. We can see from Fig. 20 that as the value of R_c moves from the switching point, the actual threshold will be close to the linear instability threshold.

As R_c is increased, the oscillatory modes become present in the linear instability thresholds. The results for R_c=20 and R_c=30 in Figs. 22 and 23, respectively, are presented. Fig. 22, shows Rayleigh numbers for R_c=20, with solutions for Eqs. (17)-(19) and (34)-(36), which produced the following stability results: Ra_L=331.65, Ra_E= 57.31, Lx=2.5 and Ly=1.8. The difference between the critical Rayleigh numbers of linear and nonlinear theories is considerable, with Fig. 22 showing that for Ra=290, Ra=299, R^2=308 and Ra=312 the solutions achieve the basic steady state soon and satisfy the convergence criterion at τ=2.72325, τ=3.16905, τ=3.83985 and τ= 4.30165, respectively. Moreover, for Ra=327 the solutions do not satisfy the convergence criterion and the program stops at τ=6, but it is clear that the solutions can achieve the convergence criterion on the next occasion. Furthermore, for Ra=330, the solutions could not reach any steady state and the program did not progress beyond τ=6. For Ra=330, the convection behaviour oscillated and access to a stable state was impossible. In Fig. 23, the value of R_c was 30. As previously mentioned, as the value of R_c increases, the linear instability threshold converges from the actual threshold; however, the behavior of the solutions becomes more oscillated.

CONCLUSIONS

We have explored double diffusive convection in porous media with vertical magnetic field, chemical reaction and variable gravity effects. Regions of very large subcritical instabilities, i.e., where agreement between the linear instability thresholds and nonlinear stability thresholds is poor, are studied by solving for the full three-dimensional system. The results indicate that the linear threshold accurately predicts the onset of instability in the basic steady state. However, the required time to arrive at steady state increases significantly as the Rayleigh number tends to the linear threshold.

Numerically, convection has three different patterns. The first picture, where R^2 is less than Ra_L, is that the solution perturbations

vanish, sending the solution back to the steady state, before the linear thresholds are reached. The required time to arrive at the steady state increases as the value of R^2 increases. The second picture, where R^2 is close to Ra_L, is that solutions can tend to a steady state, which is different from the basic steady state $\bar{v}=(0, 0, 0)$. In the third picture, where $R^2>Ra_L$, the solution does not arrive at any steady state and oscillates.

REFERENCES

1. D. A. Nield and A. Bejan, Convection in Porous Media, 4th Ed., Springer-Verlag, New York (2013).
2. P. Ganesan and R. K. Suganthi, *Korean J. Chem. Eng.*, **30**, 813 (2013).
3. I. G. Hwang, *Korean J. Chem. Eng.*, **30**, 1023 (2013).
4. M. C. Kim, *Korean J. Chem. Eng.*, **30**, 831 (2013).
5. M. C. Kim, *Korean J. Chem. Eng.*, **30**, 1207 (2013).
6. M. C. Kim and C. K. Choi, *Int. J. Heat Mass Transfer*, **71**, 313 (2014).
7. Q. Liu, D. Shen, R. Xiao, H. Zhang and M. Fang, *Korean J. Chem. Eng.*, **30**, 613 (2013).
8. M. Lungu, J. Sun, J. Wang, Z. Zhu and Y Yang, *Korean J. Chem. Eng.*, **31**, 1148 (2014).
9. D. A. Nield and A. V. Kuznetsov, *Transp. Porous Media*, **98**, 713 (2013).
10. D. A. Nield and A. V. Kuznetsov, *Transp. Porous Media*, **100**, 83 (2013).
11. D. A. Nield and A. V. Kuznetsov, *Transp. Porous Media*, **100**, 101 (2013).
12. D. A. Nield and A. V. Kuznetsov, *Transp. Porous Media*, **102**, 1 (2014).
13. D. A. Nield and A. V. Kuznetsov, *Transp. Porous Media*, **102**, 15 (2014).
14. N. Sharma, A. Dhiman and S. Kumar, *Korean J. Chem. Eng.*, **31**, 754 (2014).
15. M. Shojaeian and S. M. N. Shojaee, *Korean J. Chem. Eng.*, **30**, 823 (2013).
16. A. J. Harfash, *Ricerche Mater.*, **63**, 1 (2014).
17. A. J. Harfash, *Ann. Henri Poincaré* (2014), DOI:10.1007/s00023-013-0307-z.
18. A. J. Harfash, *Anal. Math. Phys.*, **3**, 163 (2013).
19. A. J. Harfash, *Transp. Porous Media*, **103**, 361 (2014).
20. A. J. Harfash, *Transp. Porous Media* (2014), DOI:10.1007/s11242-014-0394-4.
21. S. K. Jena, S. K. Mahapatra and A. Sarkar, *Transp. Porous Med.*, **98**, 103 (2013).
22. B. Chen, A. Cunningham, R. Ewing, R. Peralta and E. Visser, *Numerical Methods for PDEs*, **10**, 65 (1994).
23. B. J. Suchomel, B. M. Chen and M. B. Allen, *Transp. Porous Med.*, **30**, 1 (1998).
24. M. C. Curran and M. B. Allen, *Adv. Water Res.*, **13**, 70 (1990).
25. R. E. Ewing and S. Weekes, *Numerical methods for contaminant transport in porous media*, Marcel Decker, New York, **202**, 75 (1998).
26. F. Franchi and B. Straughan, *Adv. Water Res.*, **24**, 585 (2001).
27. A. Ludvigsen, E. Palm and R. McKibbin, *J. Geophys. Res.*, **97**, 12315 (2001).
28. A. Gilman and J. Bear, *Transp. Porous Med.*, **23**, 275 (1996).
29. J. Ni, C. Beckerma and T. F. Smith, *Effect of an electromagnetic field on natural convection in porous medium*, Fundam Heat Transf Electromagn Electrost Acoust Field ASME HTD (1993).
30. P. M. Patil and P. S. Kulkarni, *Int. J. Therm. Sci.*, **47**, 1043 (2008).
31. F. S. Ibrahim, A. M. Elaiw and A. A. Bakr, *Communications in Nonlinear Science and Numerical Simulation*, **13**, 1056 (2008).
32. B. Straughan, *The energy method, stability, and nonlinear convection*, Springer, *Series in Applied Mathematical Sciences*, **91**, 2nd Ed. (2004).
33. A. J. Harfash, *Int. J. Engng. Sci.*, **74**, 91 (2014).
34. A. J. Harfash, *Transp. Porous Media*, **101**, 281 (2014).
35. A. J. Harfash, *Appl. Math. Comput.*, **227**, 92 (2014).
36. A. J. Harfash, *Transp. Porous Media*, **102**, 43 (2014).
37. A. J. Harfash, *Acta Mechanica Sinica*, **30**, 144 (2014).
38. A. J. Harfash, *Three dimensional simulations and stability analysis for convection induced by absorption of radiation*, *Int. J. Numer. Methods for Heat and Fluid Flow* (2014).
39. A. J. Harfash, *J. Non-Equilib. Thermodyn.* (2014), DOI:10.1515/jnet-2014-0009.
40. A. J. Harfash and A. K. Alshara, *Three dimensions simulation for the problem of penetrative convection near the density maximum*, *J. of Hydrodynamics* (2014).
41. A. J. Harfash and A. A. *Int. J. Heat Mass Trans.*, **72**, 609 (2014).
42. G. P. Galdi and B. Straughan, *Arch. Rational Mech. Anal.*, **89**, 211 (1985).
43. P. H. Roberts, *An introduction to magnetohydrodynamics*, Longman, London (1967).
44. M. Fabrizio and A. Morro, *Electromagnetism of continuous media*, Oxford University Press, Oxford (2003).
45. S. Chandrasekhar, *Hydrodynamic and hydromagnetic stability*, *Dover*, New York (1981).
46. B. Straughan and A. J. Harfash, *Microfluid Nanofluid*, **15**, 109 (2013).